



Mechanical performance and microstructure of the grade 91 stainless steel produced *via* Directed Energy deposition laser technique

S. Samuha^{a,b,*}, J. Bickel^a, T. Mukherjee^c, T. DebRoy^c, T.J. Lienert^d, S.A. Maloy^e, C.R. Lear^f, P. Hosemann^{a,*}

^a University of California, Berkeley, Department of Nuclear Engineering, CA, 94720, the United States of America

^b Department of Materials engineering, NRCN, P.O. Box 9001, Beer-Sheva 84190, Israel

^c Department of Materials Science and Engineering, The Pennsylvania State University, University Park, PA 16802, United States

^d Optomec, Inc. Albuquerque, NM 87109, the United States of America

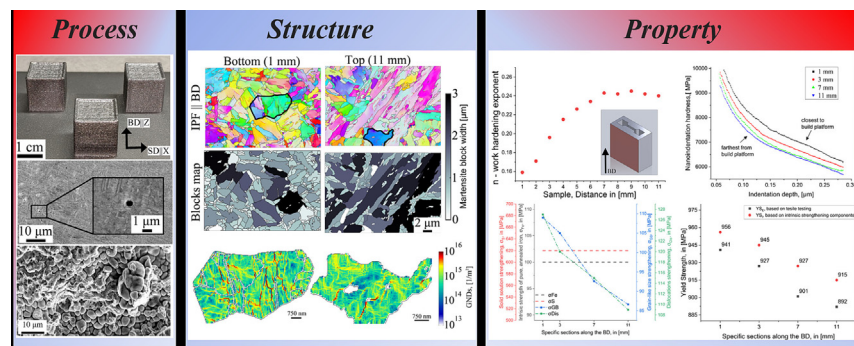
^e Reactor Materials and Mechanical Design, Pacific Northwest National Laboratory, Richland, WA 99354, the United States of America

^f MPA-CINT, Los Alamos National Laboratory, Los Alamos, NM 87545, the United States of America

HIGHLIGHTS

- Current research explores the possibility of Laser-Direct Energy Deposition (L-DED) technology being used for the F/M grade 91 steel fabrication.
- Intrinsic effects of the L-DED process were studied utilizing advanced crystallographic methods coupled with *in-situ* or *ex-situ* macro to nano-scale mechanical experiments.
- Tensile and hardness properties of the as-built L-DED-grade 91 product are superior to those of the traditional wrought material and as-deposited laser powder-bed fusion products.
- Gradual softening along the build direction was explained in the context of several competing strengthening mechanisms, and their activity was considered owing to fabrication-related mechanisms.

GRAPHICAL ABSTRACT



ARTICLE INFO

Article history:

Received 3 October 2022

Revised 13 February 2023

Accepted 28 February 2023

Available online 3 March 2023

Keywords:

Laser Additive manufacturing

Ferritic/Martensitic Steel

Mechanical properties

Nuclear components

ABSTRACT

The grade 91 ferritic/martensitic steel is considered a promising structural or cladding material for various nuclear reactor applications. Here, grade 91 was fabricated *via* the Directed Energy Deposition Laser technique. This alternative manufacturing process potentially enables tailoring of the mechanical properties through increased control of the product's microstructure.

Aimed at linking fabrication to performance *via* defining the process-structure-property relationships, the current research includes macro and up to nano-scale mechanical testing using microhardness, tensile, and *in-situ* nanoindentation hardness, coupled with electron diffraction-based microstructure characterization. Mapping of the product structure and properties was conducted by testing miniature-sized samples, parallel to the built direction ('Z' direction) and perpendicular ('X' direction) at constant distances.

We found the majority of the microstructure consists of fine and coarsened-size lath-type martensite grains, with up to 15% δ -phase, preferentially observed at the melt pool boundaries. Most intriguing was

* Corresponding authors.

E-mail address: samuha@post.bgu.ac.il (S. Samuha).

the gradual decrease found in observed metallurgical pores alongside softening at farthest distances from the cold build platform. Here, these changes were successfully explained in terms of phase composition, 'grain-like' size effects of the lath-type martensite, and geometry necessary dislocation density. In finalizing this work, several competing strengthening mechanisms were addressed, and their activity was considered owing to fabrication-related mechanisms.

© 2023 The Authors. Published by Elsevier Ltd. This is an open access article under the CC BY license (<http://creativecommons.org/licenses/by/4.0/>).

1. Introduction

High-performance Ferritic/Martensitic (F/M) stainless steels such as the modified grade 91 and its variants (P91, P92, NF616), EUROFER, and F82H, have been considered promising candidate structural materials for fast reactors and several advanced nuclear power production applications [1–3].

These components demand a unique combination of high strength, high resistance to creep, and good ductility. The modified 91 (9Cr1MoVNb), a Ferritic-Martensitic (F/M) steel, is a member of the second generation of elevated-temperature high-chromium steels.

Known for its outstanding void/cavity swelling resistance against neutron irradiation [4,5], adequate thermal conductivity, and low thermal expansion coefficients, grade 91 is considered for nuclear reactors components. Grade 91 is now used in medium temperature regimes (up to 650 °C) piping in coal-fired power plants and other applications [6,7]. However, the F/M steels are also associated with some drawbacks that hinder their assimilation as a component in fast reactors. That includes the negative effects of higher temperatures on the mechanical properties (creep-rupture strengths) [6–8]. The loss of long-term creep strength of the grade 91 steel is associated with the presence, nucleation, and growth of detrimental phases. In [9], a substantial loss of creep strength of the grade 91 steel was attributed to coarsening of chromium-rich $M_{23}C_6$ -type precipitates, significant precipitation, and coarsening of intermetallic Laves phases, and the recovery of tempered martensitic lath structure. In [10], the presence of residual δ ferrite in the initial microstructure was found to be the major cause of premature loss of creep strength in the long-term creep test. Studies have shown that higher performance of F/M steels is obtained *via* altering the microstructure and composition using various manufacturing processing strategies and by normalizing and tempering treatments [11]. For example, in [12], the T91 steel was thermo-mechanically treated by equal channel angular extrusion, which led to microstructural refining, and in turn, was found as an effective procedure to improve the combination of strength and ductility.

Additive Manufacturing (AM) technology has the potential to fabricate high-quality products in component form with tailored physical and mechanical properties *via* microstructural engineering. Laser-based AM (LAM) technologies have shown promise as potential manufacturing processes for parts in nuclear applications and reactor components [13]. L-PBF manufacturing technology, such as the selective laser melting (SLM) processes, has the capability of economically producing nuclear-grade metals ([14–18]). Classically, SLM uses a powder-bed, where a metallic powder is dispensed and fused layer by layer by a laser into a complete 3D product. The powder bed fusion process is notable for its ability to build without supports or substrates, as the powder bed itself can support overhangs or discontinuities during manufacturing. Moreover, fabrication of near net shape complex components by L-PBF is possible by printing a dedicated lattice-like support structure. However, this method has several limitations; including 1) low process efficiency, as it requires more feedstock material, and that the whole setup must undergo a thor-

ough cleaning process to switch metal powders, 2) one is tied to the tray size, and 3) balling phenomenon or fusion defects caused by printing using a non-optimized set of fabrication parameters. An alternative to the L-PBF is the Directed Energy Deposition (DED), where the raw metallic materials (either powder or wire) are injected/fed through a nozzle directly into the laser weld pool, thus, leading to a higher deposition rate and process efficiency compared to the L-PBF technique [19]. Potentially, the L-DED method is much easier to scale to larger part sizes, as there is no size restriction from the powder bed. Also, L-DED is well suited for producing functionally graded materials because different powders can be fed through one or more nozzles via a multi-hopper system [13,20–22].

The current study aims to explore the possibility of L-DED technology being used for the F/M grade 91 steel fabrication. Thus, the objectives of this study are first, to additively manufacture a grade 91 product that is at least comparable to its wrought equivalent in terms of structure and properties in the as printed state, and second, to investigate the intrinsic effects of the L-DED process on the microstructure and mechanical behavior of grade 91. To that end, comparative investigations were conducted using miniature samples machined at constant distances parallel and orthogonal to the build direction (BD) of the L-DED-T91 product. The research involves macro to nano-scale properties measured using tensile, microhardness, and *in-situ* nanoindentation experiments. The variations in the mechanical properties of the L-DED-grade 91 steel were then explained in the context of their fundamental characteristics, including microstructure and defects, by employing various electron microscopy characterization methods.

2. Experimental procedure

2.1. Product fabrication

Grade 91 product was processed at Optomec (Albuquerque, NM) under proprietary parameters. The feedstock powder was sourced from Praxair Surface Technologies (Indianapolis, IN). The feedstock powder was produced by atomization and the size range was $-100/+325$ mesh (44 to 150 μm , D_{50} was ~ 78 μm) determined by laser scattering. characterized by a small average particle size of 23 μm . The feedstock powder and AM product composition are listed in Table 1. Compared to select composition measurements of the AM product provided by Luvak Inc., carbon and sulfur compositions were measured via combustion infrared detection under ASTM standard E 1019–18. Nitrogen composition was measured via inert gas fusion under ASTM standard E 1019–18. Other elements were measured via direct current plasma emission spectroscopy under ASTM standard E 1019–18. The products were fabricated using the recommended default optimal set of parameters to the Optomec LENS MR-7 ADDITIVE model.

The AM product was fabricated in a cuboid shape with dimensions $1.5 \times 1.5 \times 1.5$ cm, on a mild steel substrate. No Cr content was found in the substrate close to the interface with the product, and overall, a change in the chemical composition throughout the product was not noted. Thus, pointing to lack of mixing effects of the powder alloy with the substrate material. The scanning was

Table 1
Grade 91 Nominal element composition (by wt.%) of the feedstock powder, and compared to that published in ASTM A387 [23].

Element (wt.%)	C	Mn	P	S	Si	Cr	Mo	Ni	V	N	Al	Co	Cu	Nb	Fe
LAM powder	0.078	0.44	<0.002	0.002	0.38	9.00	0.95	0.037	0.18	0.057	0.0052	0.017	0.018	0.077	Bal.
ASTM [23]	0.08–0.12	0.30–0.60	Max. 0.02	Max. 0.01	0.20–0.50	8.00–9.50	0.85–1.05	Max. 0.4	0.18–0.25	0.03–0.07	Max. 0.02	–	–	–	Bal.

conducted alternately in the x and y directions, and a contour was used for each layer. The general view, cross-section, and top-view of the test prints are shown in Fig. 1 (a–c), noting that the 'BD' and the 'SD' are the build and scanning directions, respectively.

2.2. Mechanical testing

The influence of build orientation was evaluated using Vickers microhardness, *in-situ* nanoindentations, and tensile testing. The Vickers testing (Wilson microhardness tester) was conducted on the BD-SD plane, following typical mechanical grinding and polishing. Hardness measurements were conducted at ambient temperature and normal pressure conditions under 1.5 Kgf/ 15 s loading conditions. The indents were locally spaced to both the edges and other neighboring indentations by at least five times the Vickers diagonal length of an indent.

Sequential sections from the cuboid-shaped product were cut and machined using EDM to miniature dog bone-shaped tensile specimens - SSJ-3 type with a gauge section of $5.0 \times 1.2 \times 1.0$ mm.

The tensile samples were extracted along two orientations - parallel and orthogonal to the BD (BD \parallel Z), as depicted in Fig. 1 (d). These two types of samples are referred to in the current work as 'X' (SD-BD plane), and 'Z'-type (SD-SD plane) specimens. 13 sequential sections of X and 11 sequential sectors of Z-type specimens were studied. After EDM cutting, the samples were mechanically polished to remove any residual debris left from the machining. Uniaxial quasi-static tensile tests at room temperature (25 °C) were carried out on the Kammrath and Weiss *in-situ* tensile/compression device. This system was equipped with a 5kN load cell and was loaded at 0.5 μ m/s. Fractography analysis of

specific specimens was carried out using scanning electron microscopy (SEM) to identify the fracture mode and study the printed product's inner-macro structure.

To assess the nano-scale properties of the L-DED grade 91 product, *in-situ* nano-indentation experiments in an SEM were performed on a FemtoTools NMT04 Nanomechanical Testing System. Prior to nano-indentation experiments on the grade 91 specimens, the system was calibrated at depths of interest using a certificate fused quartz. The depth-control indentation was used in the continuous stiffness mode (CSM, [24,25]) with the maximum indentation depth being 350 nm, indents were locally spaced by 5–7 μ m. The indentation hardness, reduced modulus, and load-depth data were extracted and analyzed employing the Oliver-Pharr method [25]. In the current work, Young's modulus was derived from the reduced modulus (E_r) using the following relation –

$$\frac{1}{E_r} = \frac{1 - \nu^2}{E} + \frac{1 - \nu_i^2}{E_i} \quad (1)$$

where ν and E are Poisson's ratio and Young's modulus, and the ν_i , E_i are those for the diamond indenter (0.07 and 1141GPa, respectively). The Vickers Hardness (H_v , [Kgf/ mm^2]) and yield strength ($\Delta\sigma_{y,s}$, [MPa]) were also obtained from nanoindentation hardness measurements by using the following empirical correlations, where H_0 was used as $H_{\text{Berkovich}}$. This approach was also outlined in previous work [26,27,26,28,29]

$$H_v [\text{Kg/ mm}^2] = 0.0945 \cdot H_{\text{Berkovich}} [\text{GPa}] \cdot 1000 \quad (2)$$

$$\sigma_{y,s} [\text{MPa}] = 2.82 \cdot H_v [\text{Kg/ mm}^2] - 114 \quad (3)$$

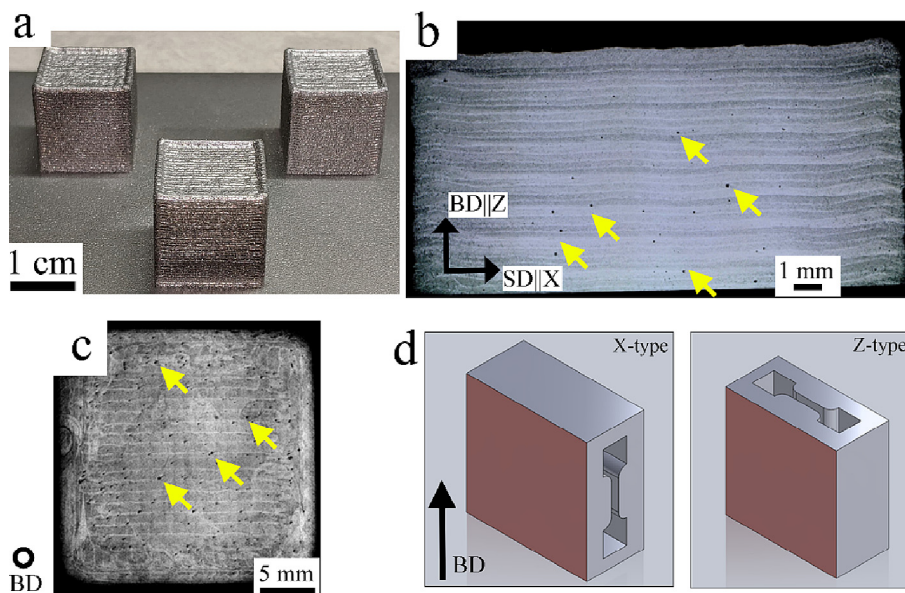


Fig. 1. (a–c) Photographic images of the cuboid additively manufactured by DED-SLM from grade 91 steel powder. The yellow arrows mark pores in the build. (d) Schematics illustration of specimen's extraction for tensile tests. Noting that the BD and the SD are the build and scanning directions, respectively. (For interpretation of the references to color in this figure legend, the reader is referred to the web version of this article.)

2.3. Microstructural characterization

For metallographic examination, the surfaces of the samples were mechanically ground and polished, followed by chemical-mechanical polishing using the VibroMet™ 2 Vibratory Polisher (Buehler) for 1.5 hr using a final polishing media of 0.06 µm diameter colloidal silica. Then, the samples were electro-polished using 10 % oxalic acid at 6 V and 0.200 [Amp] for 3 s.

Microstructure analysis was carried out using the Thermo Scientific Scios 2 DualBeam SEM, coupled with the symmetry electron back-scattered diffraction (EBSD) detector (Oxford Inc.). The MTEX package (v. 5.8) was employed for post-processing and visualization of the EBSD data [30]. The grain-boundary character distribution was categorized based on misorientation angle criteria – misorientation angles 2–5°, 5–15°, and 15–62.5° were categorized as low, medium, and high angle grain boundaries (LAGBs, MAGBs, and HAGBs), respectively. Band Slop (BS) map was used for phase discrimination. The BS is a measure of pattern quality and is evaluated as the maximum slop of intensity at the edge of the bands in the EBSD pattern. Thus, a high BS value describes a high-quality EBSD pattern [31]. Reconstruction of the prior austenite (γ) microstructure was carried out employing the variant graph approach in the ORTools package (V.2, [32]). The initial guesses for the parent-to-child orientation relationship (OR) were the Nishiyama-Wassermann (N–S), the Greninger-Troiano (J–T), and the Kurdjumov–Sachs (K–S) ORs. The latter was chosen based on the lowest misfit between the grain misorientations and the misorientation of the OR. Geometrically Necessary Dislocations (GNDs) density (ρ) was extracted by calculating the curvature components [33], a method based on the work pioneered by Nye [34] and Pantleon [35]. Grain-averaged GNDs density ($m(\rho)$) was calculated for each map based on a lognormal fitting, using the following equations:

$$f(\rho|\mu, \sigma) = \frac{1}{x\sigma\sqrt{2\pi}} \exp\left(-\frac{(\ln(\rho) - \mu)^2}{2\sigma^2}\right) \quad (4)$$

$$m(\rho) = \exp\left(\mu + \frac{\sigma^2}{2}\right) \quad (5)$$

Where $m(\rho)$ is the grain-averaged value of GND density, and σ and μ are the scale and location parameters of the lognormal distribution. Full mathematical description of the grain-averaged GNDs density calculation can be found in [33–35]. In the current study, all calculation and analysis of the grain-averaged GNDs density were performed utilizing the MTEX toolbox, according to Pantleon and Nye theory ([34,35]). This Methodology for assessing the GNDs density was successfully used in various alloys and different deformation states ([36–38]).

3. Results

3.1. L-DED grade 91 microstructure

The grade 91 product in the as-built state included many defects sites; some of these defects are represented by yellow-colored arrows in Fig. 1 (b), and (c). Overall, the defects are nonuniformly distributed; their size and number substantially decrease along the BD. Fig. 2 (a) and (b) depict higher-magnifications SEM images focusing on defects found at the bottom and top surfaces of the product, respectively. Regardless of their location in the product, all defects show spherical morphology, commonly associated with intralayer (metallurgical) pores formed due to trapped gases or gases that evolved from the powder during consolidation. Other AM-related defects, such as keyhole pores, designated by their irregular shapes, were not noticed. The better densification (*i.e.*,

decrease size and number of pores) farther away from the cold built platform might have a detrimental effect on the mechanical properties. This will be addressed later on in this study.

A general description of common microstructure characteristics of all specimens is given in Fig. 3, using EBSD-based band-slop (BS), and IPFs maps. The IPF maps are colorized according to the crystallographic orientation aligned with the built direction. The IPF maps are superimposed with grain boundaries (GBs) designated by local misorientations, a legend describing the GBs' characteristics is depicted in the right corner of Fig. 3. Three colonies of grains differentiated by morphology were noticed. The first and the second group are martensite grains with a refined or coarsened prior austenite grain (PAGs) structure; see zone A and B in Fig. 3, respectively. While the coarsened-sized grains are identified by a textbook-like microstructure of the lath martensite (*i.e.*, blocks, packets, and laths), the fine-sized grains, limited by their size, show only a small number of blocks with boundaries, which are difficult to be recognized and categorize. The third group is polygonal-shape grains, showing much lower lattice distortions and smaller intragrain angular misorientation compared to that found for the F/M phase, as interpreted from the BS map (red-colored grains in Fig. 3 (a)) and histogram, Fig. 3 (b). Considering their unique morphology and preferential formation, traced at some of the PAGBs and triple points of the F/M grains, it is plausible to assume that these are δ-phase grains. Supporting this assumption is EBSD based GNDs analysis, revealing much lower bulk GNDs density ($m(\rho)$) for the polygonal-shape grains. Plausibly, this is attributed to the leaner carbon content in the δ-phase. In this context, a much higher GNDs density was found for the F/M phase (see Fig. 3 (c)), with a $m(\rho)$ similar to that published for a commercial T91 (roughly 7×10^{14} [1/m²] [39]), also validating GNDs analysis conducted in the current research. In-situ nanoindentation hardness tests were conducted to further confirm the identity of phases. At least 14 repeats were performed, and average values are reported. To better differentiate among phases, electron channeling contrast was used. The premises of a representative polygonal-shape grain was marked using Ga⁺ ion etching followed by validation based on EBSD analysis, see Fig. 4 (a). Fig. 4 (b) and (c) are GNDs maps focused on the piled-up material at the circumferences of the phases' indentation imprints. Large lattice strain gradients and, in turn, high GNDs are noted. Later, presence is linked with the geometrical changes in the surface shape under indentation.

Fig. 4 (d) shows plots of the averaged indentation load (P) and averaged hardness (H) vs indentation depth (h) curves for the AM product. Both phases show a decrease in hardness with increasing indent depth, a depth-dependent effect known as indentation size effect (ISE) [41]. The ISE depends on deformation-induced strain gradients which induce GNDs, and in the current study, was the ISE was quantified according to the Nix-Gao relation [42] as,

$$\frac{H}{H_0} = \sqrt{1 + \frac{h^*}{h}} \quad (6)$$

where hardness value (H) corresponds to a certain indentation depth (h). The H_0 is an intrinsic parameter representing the hardness at an infinite depth (*i.e.*, macroscopic hardness), and h^* is a characteristic length parameter, which depends on the material and the shape of the indenter tip. Based on the Nix-Gao relation, the H_0 and h^* were determined from H^2 vs $1/h$ curve fitting (see Fig. 4 (e)). Results are tabulated in Table 2.

Overall, a much lower indentation depth was obtained for the F/M phase for a given load (P), pointing to F/M and the (potentially) δ as the hardest and softest phases, respectively. Also, much higher H_0 values and lower h^* were obtained for the F/M phase, thus

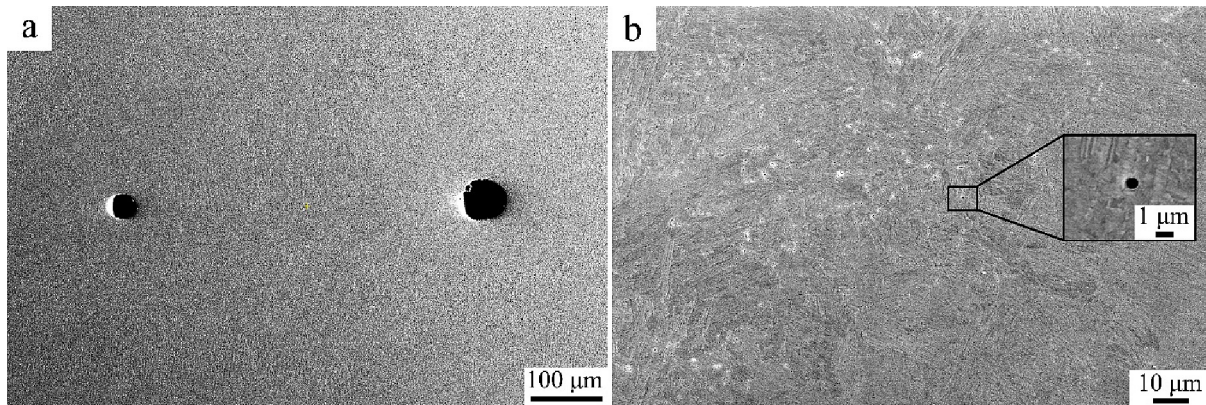


Fig. 2. Macro and micro defects (a) close to and (b) farthest away from the build platform.

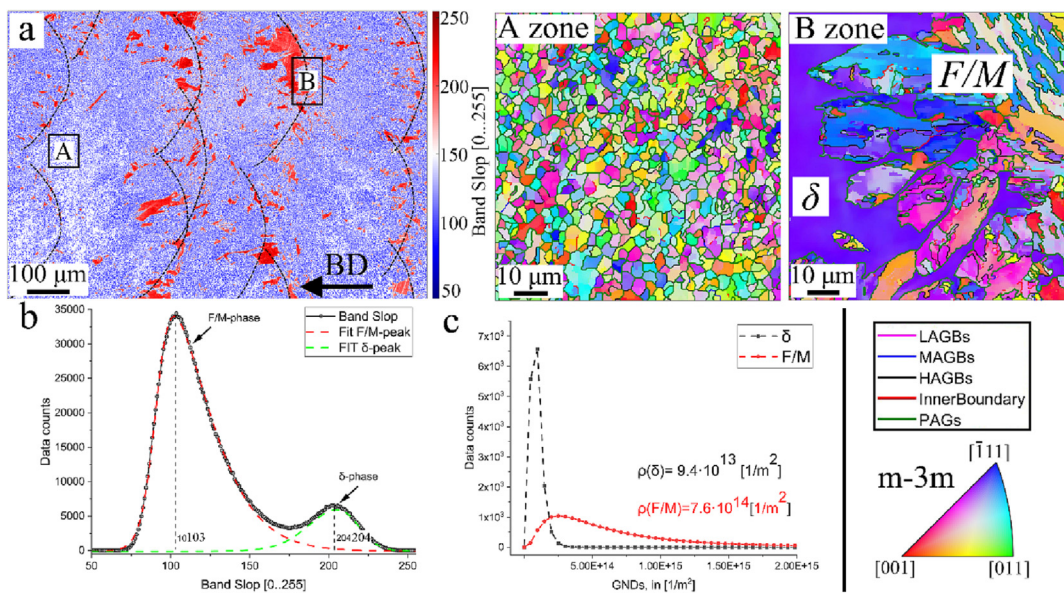


Fig. 3. Microstructure of the grade 91 product. In (a) and (b) are the band slope map and histogram, where band values are associated with the F/M and δ -phases. Zone A and B are segmented regions from (a), showing the unique characteristics of the phases. (c) is the distribution of discrete GNDs, as calculated from the segmented phases. On the bottom right corner is a legend describing the GBs' characteristics and color scheme key in the form of the stereographic triangle. The reader is referred to the web version of this paper for the color representation of this figure.

pointing to a smaller ISE for the F/M–phase, as justified by the GND analysis showing a smaller deformation zone at the circumference indent of the F/M phase (see Fig. 4 (b) and (c)). Following the above analysis, it can be concluded that the softer grains are indeed δ -phase.

In close examination of the BS map, the δ -ferrite grains are uniquely dispersed in the microstructure in a bands-like configuration that resembles the semicylindrical shapes of melt-pool boundaries (MPBs). For visual clarification, Fig. 3 (a, b) includes a highlight (dashed black lines) of areas where high-density δ -ferrite grains were observed. The volume fraction of the δ -phase was calculated through BS segmentation, and was found to be 15%. This will further be addressed in the discussion.

3.2. Micro-hardness and tensile results

Vickers microhardness measurements were taken along with and perpendicular to the BD on the BD-SD plane. No clear relationship was established between hardness values and location. Also, similar topographic surrounding (*i.e.*, deformation zone) was noticed for indents, regardless of their location or related hardness

values. The average hardness \bar{HV} and the standard deviation, S , was 349.8 ± 21 HV/1.5, significantly higher than that published for the wrought normalized and tempered T91 and grade 91 (~ 260 – 270 HV [43,44]).

Results of the tensile tests for the as-build samples are presented in Fig. 5. Representative engineering stress–strain curves, as measured from the X and Z-type specimens, are plotted in Fig. 5 (a) and (b), respectively. The data is further analyzed and reported in yield strength (YS), ultimate tensile strength (UTS), and uniform elongation in Fig. 5 (c–d).

The wrought grade 91 steel normally exhibits a low yield and ultimate tensile strength (~ 600 and ~ 730 [MPa], respectively) and moderate uniform elongation ($\sim 8\%$) [45]. The AM product, on the other hand, shows a substantial increase in strength (~ 900 [MPa]) and a slight increase in uniform elongation (10%). As appreciated from tensile results, variation in mechanical properties depending upon location was pronounced mostly for the Z-type specimens. Regardless of their origin, all specimens show medium plastic deformation accompanied by deformation hardening before final fracture, characteristics of a mix of brittle–ductile

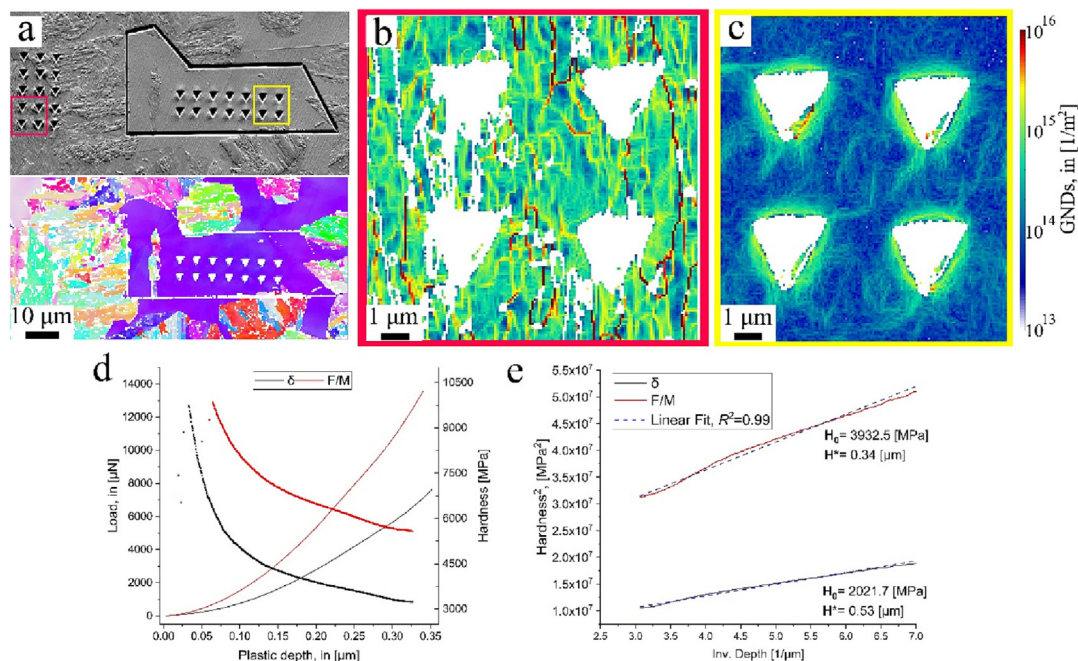


Fig. 4. Nanoindentation hardness testing of the F/M and δ -phases. In (a) is an electron channeling contrast image and EBSD-IPF (\parallel BD) where ion etched zone marks a δ grain, red and yellow squares in (a) depict indentations imprints zones from which GNDs maps of the (b) F/M (c) and δ -phases were calculated. (d) Load and nanoindentation hardness vs plastic depth, and (e) Curve fitting of experimental data for the F/M and δ -phases using the Nix-Gao relation. A color scheme key for GNDs density maps is shown in (c). (For interpretation of the references to color in this figure legend, the reader is referred to the web version of this article.)

Table 2

Results obtained from nanoindentation testing and EBSD analysis.

Phase	$E_R^{\#}$ [GPa]	H [MPa]	H_0 [MPa]	h^* [μ m]	E [GPa]	H_V [Kgf/mm ²]	$\Delta\sigma_{YS}$ [MPa]	$m(\rho)^{\textcircled{a}}$ [1/m ²]
F/M	213.2	6,426	3,932	0.34	238.3	371.6	933.9	$7.6 \cdot 10^{14}$
δ	198.7	3,812	2,021	0.53	218.7	191.0	424.6	$9.4 \cdot 10^{13}$

Similar value (219 [GPa]) was published in [40] for wrought (unirradiated) F/M T91, normalization at 1040 °C for 60 min followed by tempering at 760 °C for 60 min. **@** The nominal GNDs density was extracted from a region far from the indents, representing the ‘initial state’, prior to measurement.

material. Still, it should be noted that while Z-type specimens show a similar extent of plastic flow, X-type specimens failed at different strains. Also noticeable is a slight gradual increase in the UTS, combined with a gradual decrease in YP for the Z-type specimens, with distance from the base. Upon correlating the mechanical properties with the fabrication order, further insights are revealed through strain hardening analysis. The strain hardening exponent (n) was obtained from the slope of the true stress versus true strain curve in tensile tests, which were plotted on a logarithmic scale. In the current study, the relationship stress-strain was expressed using the following equation:

$$\sigma = k\varepsilon^n \quad (7)$$

In which σ and ε are the true stress and strain and k is the strength coefficient. The strain hardening exponent values are presented in Fig. 5 (e) and (f) for X and Z-type specimens, respectively. The X-type of specimens are characterized by the highest and very similar values of strain hardening exponent, regardless of their location, with an average (\bar{n}), and standard deviation, S , of 0.244 ± 0.01 . On the other hand, a sharp increase in the (n) was noted for the Z-type of specimens, from the bottom surface to the 7 mm distance from the built platform, followed by a plateau in the (n) values up to the top surface (11 mm). Following this analysis, better uniformity in mechanical behavior, such as higher plasticity, is expected with a farther distance from the heated base.

Further analysis regarding the effects of the fabrication procedure on the microstructure and properties is presented in the following sections.

3.3. Fracture surface analysis

A clear relationship between specimen origin (orientation and/or order) with fracture feature or mode was not found. Therefore, the description in this section is considered for all specimens.

Representative macrographs of the fracture surface are exemplified in Fig. 6. From macro-perspectives, the fracture surface reveals large-sized pores (Fig. 6 (a)), which are expected as previously described in the current work. Other characteristics of the fracture surface are regions with a high density of small dimples (Fig. 6 (b)) or pseudo-cleavage facets (Fig. 6 (c)), implying a ductile–brittle mix fracture mode. The morphology of the dimples resembles fine-size grains found at the melt pools; see zone A in Fig. 3. These dimples result from microvoids nucleation followed by their rapid coalescence at HAGBs, and it is therefore believed that these regions promote rapid intergranular fracture. On the other hand, regions showing pseudo-cleavage facets correlate with the brittle characteristics of the martensite phase found mostly at the MPBs (zone B, in Fig. 3). At these regions, dominantly sharp cracks, designated by red arrows in Fig. 6 (b-d), propagate along PAGBs, and deflect, presumably in conjunction with packet boundaries. Secondary grain boundary cracks were also observed, and they are indicated by green arrows in Fig. 6 (b-d).

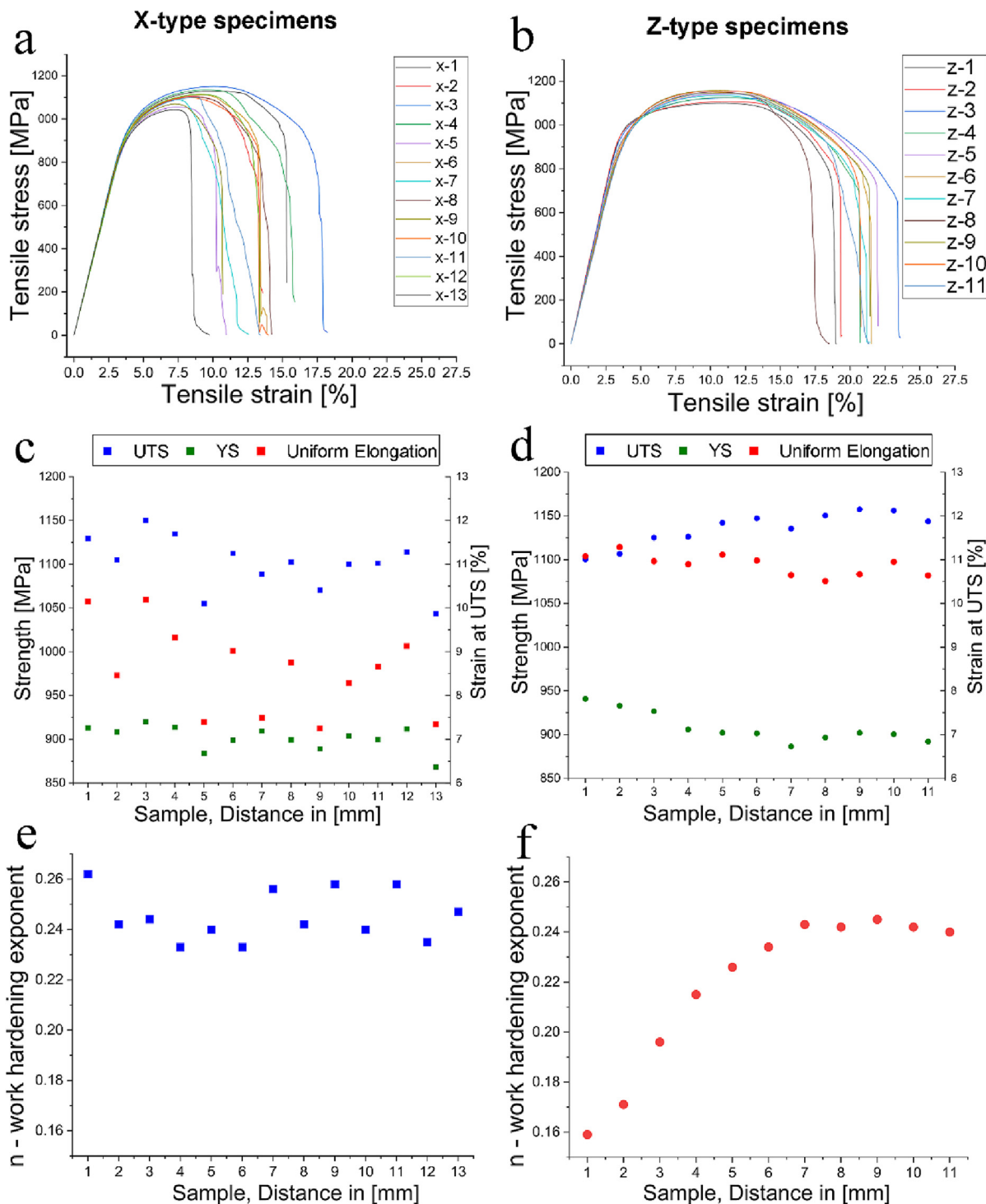


Fig. 5. Quasi-static tensile test, (a, b) typical engineering strain–stress curves, (c, d) YP, UTS and uniform elongation, (e, f) work hardening exponent, from the cubes and orientations, as illustrated in Fig. 1.

Apart from the features mentioned above, the fracture surface of the AM product included powder particles, as depicted in Fig. 6 (e) and (f). Their shape, spherical or asymmetric, points to fabrication defects – lack of fusion and partial dissolution resulting from low energy density.

As it appears from the tensile testing, only subtle fluctuations in the mechanical properties were noticed perpendicular to the building direction (X-type, BD-SD plane). In contrast, significant changes were noted for samples differentiated by their distance along the

build direction (Z-type, SD-SD plane). To better understand these changes, a correlative study was conducted through nano-scale mechanical properties measured using *in-situ* indentation experiments coupled with electron diffraction analysis. This investigation was focused on four Z-type samples chosen based on their tensile properties and are designated by their distance from the cold build platform: 1, 3, 7, and 11 mm. Fig. 7 (a) shows the indentation-depth dependence of the nanoindentation hardness of the product. Each plot symbolize data of at least eight indents. Fig. 7 (b) depicts

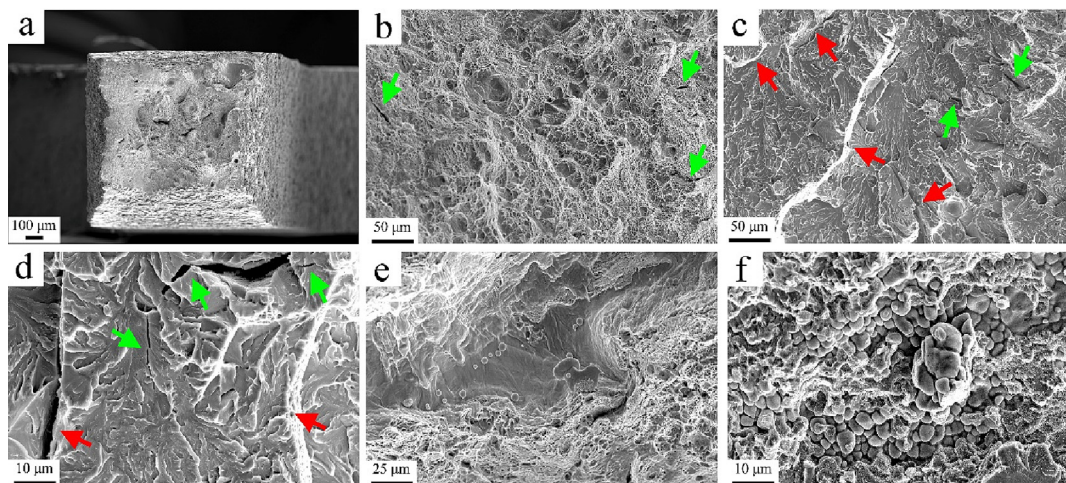


Fig. 6. Fractography of grade 91 in the AB state showing (a-c) typical martensite structure, low to high magnifications showing cleavage surface and transgranular cracks, and (d-f) defects (macro-porosity, lack of fusion, and nonmelted feedstock powder) promoting failure.

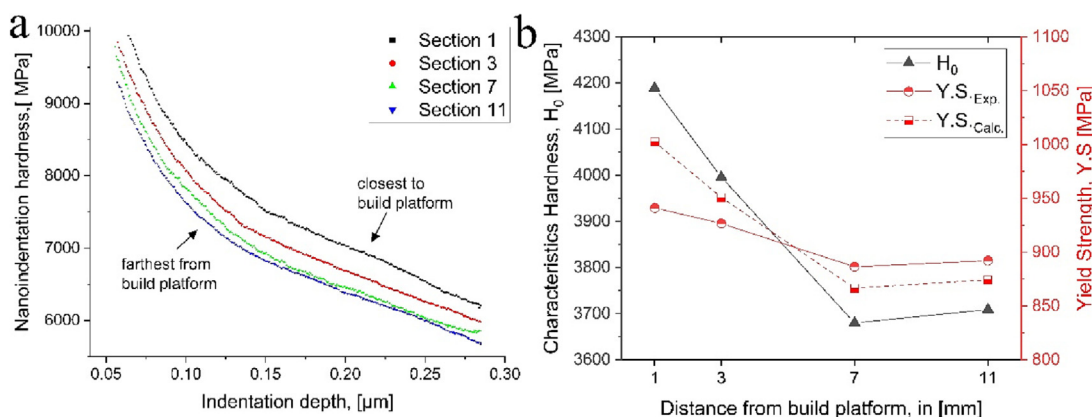


Fig. 7. Micro and nano mechanical properties of specific DED-grade 91 samples along the BD. In (a), Indentation-depth dependence of the averaged nanoindentation hardness, and in (b), averaged characteristic nanoindentation hardness, experimental and calculated yield strength.

the indentation-depth dependence of the averaged characteristic nanoindentation hardness (\bar{H}_0), as obtained along with the built platform. The \bar{H}_0 values were extracted from a linear region of 170–290 [nm] penetration depth in the Nix-Gao plots. An obvious decrease in the \bar{H}_0 is noticed with distance from the built platform. Superimposed on Fig. 7 (b) are the experimental YS values obtained from the miniature tensile experiments and the calculated YS values using Eq. (1) and (2). Results are also tabulated in Table 3, including $\Delta \sigma_{YS}$, which are the differences between the experimental calculated YS values for each test case. A similar trend is clearly noticed in the plots of the \bar{H}_0 and the YS. Also, the calculated YS's from nanoindentation measurements are in good agreement (mean error < 3.3 %) with the tensile test results,

thus validating the results obtained via nanoindentation experiments.

Both nanoindentation hardness and tensile tests point to softening on the micro and nano-scale, that might be attributed to microstructure evolution with farther distances from the cold build platform. To explore further this possibility, PAGs reconstruction and GNDs analysis were conducted on the selected 'Z'-type samples.

Both the block and packet are bounded by high tilt boundaries, thus both hinder dislocation mobility during plastic deformation. As the block width is much smaller compared to the packet size, it is plausible to assume that high angle boundaries are dominated by the block boundaries. Therefore, owing to their dominated key structural parameter, the current research considers block size as

Table 3
Nanoindentation and tensile testing results of specific DED-grade 91 samples along the BD.

Distance from the build platform [mm]	H_0 [MPa]	H_V [Kgf/mm ²]	σ_{YS} [MPa]		$\Delta \sigma_{YS}$ [%]
			Calc.	Exp.	
1	4,189	396	1,002	941	6.5
3	3,996	378	950	927	2.6
7	3,680	348	867	886	2.2
11	3,709	351	874	892	1.9

the “effective grain size” for strength. In that context, the martensite block widths were calculated based on the habit plane orientation of laths forming the block [46]. It should be noted that PAGs might also contribute to strengthening, however, as the current research did not include subsequential heat treatment to fabrication (*i.e.*, normalizing and tempering), we expect that the overall contribution of PAGs to the strengthening is roughly the same regardless to specimen origin. Fig. 8 (a, b) depicts the ‘grain-like’ size distribution plots and IPFs (||BD) maps showing the microstructure closest to and further away from the built plate, respectively. While the overall martensite structure looks similar, an increase in the block’s width were noticed farthest away from the build platform whereas both PAGs and packets do not scale-up with the block’s width. Above results point to the strong effects of the cold platform build strategy on the gradual changes in the block width, and in turn, on the gradual softening.

An EBSD based GND analysis was performed in specific samples along the BD, results are presented in Fig. 9 in the form of distribution of discrete GNDs, alongside GNDs maps of segmented grains at close distance to the build platform (1 mm) and farthest away (11 mm).

These grains were chosen based on their similar size and are marked using a black line in Fig. 8 (b).

Prior to quantitative analysis, the uncertainty of the EBSD-measured GNDs density was determined. Here, the lower bound GNDs density sensitivity (ρ_{min}^{GNDs} , *i.e.*, ‘noise floor’) was determined, following the work by Wilkinson and Randman [47], as follows:

$$\rho_{min}^{GNDs} = AR/b \cdot SZ \quad (8)$$

where, the AR is the angular resolution *i.e.*, the uncertainty in the orientation measurements. To assess the AR, a reference silicon single crystal was tested with the Symmetry S2 CMOS EBSD detector, that was used throughout the current research. Employing an adopted methodology from a recent publication by Lehto [48], the AR was found equal to 0.012° ($2.1 \cdot 10^{-4}$ radians). The *b* stands for the Burgers vector, which equals 2.482 Å for the grade 91 steel, and the *SZ* is the step size, which was 0.15 µm, providing extremely high spatial and angular resolutions to better evaluate fine details of the dislocation’s structures [49]. With these values, the uncertainty in GND density calculations was found to be $\sim 5.6 \cdot 10^{12} [m^{-2}]$. An average GND density of $\sim 7.9 \cdot 10^{14} [m^{-2}]$ was calculated from all specific sections along the BD (‘datasets’). This value is significantly higher than the lower bound GNDs density sensitivity, and therefore, it is sufficiently reliable to qualitatively analyze the distribution of GND density using these datasets.

A gradual decrease in the GNDs density with distance from the build platform was noticed, a result which is in line with the mechanical softening along the BD. The GNDs maps of the segmented grains are composed of an ordered configuration of dislocations, distributed non-uniformly in the microstructure, mostly paved from PAGBs or packets to the grain core. The lower intensity of GNDs and larger spacing between dislocation arrays were observed at the top compared to the bottom of the product, outcomes attributed to the coarsening of the blocks.

4. Discussion

4.1. process-structure-property

The cold build platform strategy had led to gradual changes in the microstructure, which in turn are reflected in the variation in the mechanical properties. To the AM product, the built platform stands as a heat sink and, in turn, greatly affects the cooling rate in the AM product, especially closest to the substrate. It is not unlikely that a higher cooling rate closer to the build platform results in a higher density of carbon atom partitioning. These clusters are known to hinder dislocation mobility, thus increasing hardening. It is also plausible to assume that the effects of track overlapping (*i.e.*, cyclic remelting) along with the BD increases. Closest to the build platform, due to relatively faster cooling rates, newly deposited layers cool down below the *M_s* temperature prior to the deposition of a fresh layer. With farther distance along with the built platform and lower cooling rates, reheating previously deposited material during the deposition of subsequent layers promotes softening of the lath-type martensite structure, similar to tempering.

Here, the geometry of the block was found to be a key structural feature that strongly affects the mechanical properties. The very coarsening of the blocks along the BD reduces the effective barriers to dislocation slip, as indicated by the decrease in the yield strength. In addition, the coarsened structure has the capability to accommodate a higher density of mobile dislocations during plastic deformation whereas, at lower distances from the build platform, the fine structure consists of a higher density of dislocations, which hinders additional dislocation activity. This analysis is in line with the gradual increase in work hardening found along the BD.

Two major phases were identified – the tempered martensite and the δ -phase. Compared with the δ -ferrite, the tempered martensite grains displayed much higher nanoindentation hardness. This is attributed to the morphological complexity of the martensite colonies, delineated by the PAGs, comprised of a hierar-

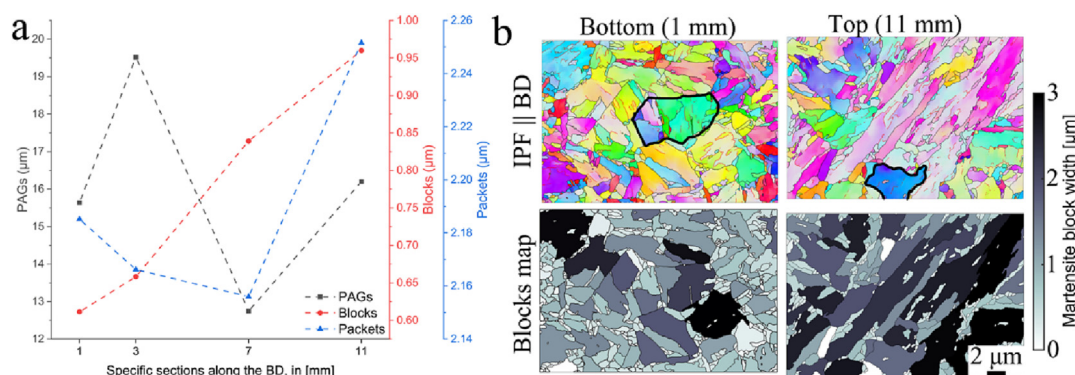


Fig. 8. Prior austenite grains reconstruction analysis. In (a) grain-like size distribution, for specific samples along the BD. (b) IPFs maps (||BD) of the child microstructure and the martensite block width map, for samples at close distance to the build platform (1 mm) and farthest away (11 mm). A color scheme key for martensite block width maps are shown to the right of (b). Marked grains in (b) are further investigated using the EBSD-GNDs analysis.

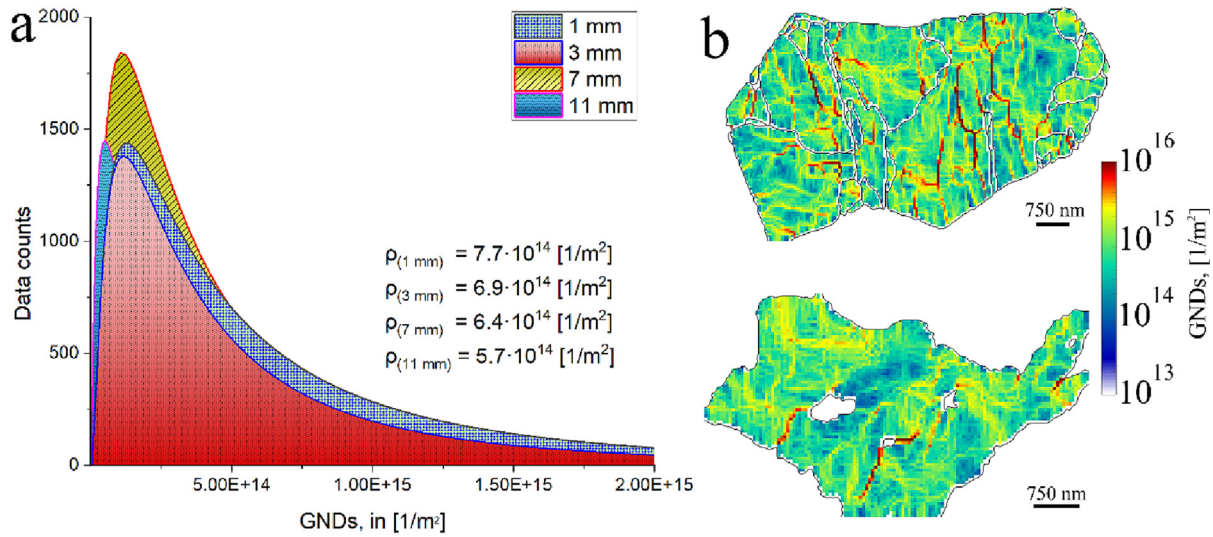


Fig. 9. EBSD-GNDs analysis. In (a) are distribution of discrete GNDs for the specific samples along the BD, (b) segmented grains at close distance to the build platform (1 mm) and farthest away (11 mm). A color scheme key for GNDs density maps is shown to the right of (b).

chical structure of packets, blocks, and laths. In addition, the martensite grains have also shown larger amounts of GNDs which is expected as the austenite usually transforms to super-saturated martensite containing a high density of dislocations. As the AM product was not tempered after the build, the recovery of excess dislocations or precipitation of carbonitrides was not obtained. Moreover, the $\gamma \rightarrow F/M$ -phase transformation also involves solute atom clustering that might also generate further resistance forces against dislocation glide.

The δ -ferrite was preferentially observed at the melt pool boundaries. One of the possible reasons for the co-existence of this phase is rapid cooling rates during fabrication (typically 10^4 °C/s). On the one hand, the (residual) δ -ferrite might result from incomplete phase transformations [50]. As an alternative, reheating of previous layers to below the solidus temperature during deposition of a new build layer might have promoted a solid-state formation of the δ -ferrite. In that case, rapid cooling rates suppressed back transformation to austenite and, subsequently, to martensite.

Retained austenite (γ') was not observed. Plausibly, the γ' -phase is destabilized by iterative reheating and subsequent rapid cooling (below M_s), which in turn promotes transformation to the martensite phase. In [51], substantial decrease in the amount of retained austenite was achieved via cryogenic soaking of the normalized P91 alloy prior to tempering treatment. Plausibly, rapid cooling during fabrication might also promote complete martensite transformation.

4.2. The collective contributions of different strengthening mechanisms

The strength of the lath-type martensite structure has been studied extensively ([52] and, [53]). The integrated strengthening of the lath martensite can be factored into a number of intrinsic components:

$$\sigma_{YS_i} = \sigma_{Fe} + \sigma_S + \sigma_{GB} + \sigma_P + \sigma_{dis} \quad (9)$$

Where, σ_{Fe} is the contribution to the overall strength from intrinsic strength of pure, annealed iron, and equals ~ 100 MPa [54], σ_{GB} is the grain-like strengthening, σ_S is the strengthening due to substitutional solutes (σ_{SS_i}) and strength increment due to dissolved carbon (σ_{SS_C}), σ_P and σ_{dis} are the contributions to strength from carbides or precipitate hardening and dislocation strengthening, respectively.

Grain-like size strengthening was assessed based on PAGs reconstruction analysis, using the Hall–Petch (H–P) relation which was found valid only for the blocks. Indeed, a linear fit with $R^2 = 0.98$ was obtained for the H–P plot of the YS vs reciprocal square root of the block width (plot not included). Thus, pointing to the strong strengthening effect of the blocks' boundaries. Their contribution to the overall strength was estimated using the following [46]

$$\sigma_{GB} = K_{H-P} / \sqrt{d_B} \quad (10)$$

Where K_{H-P} is the Hall–Petch coefficient, equals 120 MPa [55], and d_B is the equivalent block size which is taken as two times of the block width to better accommodate the planar boundaries of the blocks to that of grain boundaries in an equiaxed grain structure [46].

The solid solution strengthening induced by substitutional solute and interstitial atoms were estimated using the following [56]

$$\begin{aligned} \sigma_S &= \sigma_{SS_C} + \sum x_i \sigma_{SS_i} \\ &= 1722.5\sqrt{w_C} + 105[\text{Si}] + 45[\text{Mn}] + 37[\text{Ni}] + 18[\text{Mo}] \\ &\quad + 5.8[\text{Cr}] + 4.5[\text{V}] + 4.9[\text{Co}] \\ &= 485 + 135 = 620[\text{MPa}] \end{aligned} \quad (11)$$

where σ_{SS_C} is the strength increment due to dissolved carbon in the matrix and $\sum x_i \sigma_{SS_i}$ term represents the collective substitutional solute strengthening from (i) element, in wt.%. In this study, Cr-rich carbides or precipitates (MC and MX-type phases) were not observed in the matrix nor detected within and at the interface of the δ -ferrite (see Figure A 1- Appendix A of supplementary data), suggesting that 1) a substantial amount of the minor phases such as the $M_{23}C_6$ dissolved during the fabrication process or 2) or to reduced segregation of solute elements (such as vanadium, niobium, and carbon) due to the rapid cooling, which in turn hinders the formation of these phases. Therefore, the influence of carbide or precipitate strengthening (σ_P) was not considered in the current research. This may lead to an underestimation of the yield strength. Nevertheless, we believe that the relatively high strength increments due to solid solution strengthening from carbon atoms in the matrix as solute atoms (~ 485 MPa) convolutes to some extent the lack in precipitation strengthening.

The strengthening due to dislocations can be estimated using the following:

$$\sigma_{dis} = \alpha G b \sqrt{\rho_{tot}} \quad (12)$$

where, G is the shear modulus of pure Fe, and equals ~ 80 GPa, and $b = 2.482 \text{ \AA}$ is the Burgers vector of dislocations for the grade 91 steel. The empirical constant α relates to the dislocations' configuration. From close observation of the GNDs maps (see, for example, Fig. 9 (b)), the GNDs are arranged in well-organized ('dense') configurations, which are plausibly the starting point to grain fragmentation into sub-grains. For these energetically favorable configurations, the α is set to 0.23 [57], whereas a value of 0.3 (or higher) is usually chosen if dislocations are distributed without forming cells. The ρ_{tot} represents the sum of GNDs and statistically stored dislocations (SSD). In [37], the hardening nature of additively manufactured stainless steel was thoroughly investigated. There, a careful evaluation based on separate strengthening components and the Taylor's hardening model led to the conclusion that the majority of the total dislocations are the GNDs, and thus the mechanical properties are governed predominantly by the GND-type of dislocations. Current research adopts this approach and considers GNDs to be the dominating key structural parameters in strengthening due to dislocations, with a minor risk of underestimating the yield strength by excluding the contribution of the SSDs-type of dislocations.

The strengthening components alongside the integrated yield strength (YS_I) vs the experimental YS (YS_E) for the L-DED grade 91 steel are plotted in Fig. 10 and are also summarized in Table 4. The collective contribution of all strengthening mechanisms is closely equal to the YS_E, overestimates by only ~ 20 MPa, and with the highest error below 3 % compared to the YS_E. The above analysis clearly points to two major strengthening components, the σ_{GB}

and σ_{Dis} , both were found to be responsible for the gradual softening with increased distance from the cold build platform.

4.3. The L-DED technology being used for the F/M grade 91 steel fabrication

The tensile properties for various grade 91 steels fabricated by L-DED (this work), as-deposited laser powder-bed fusion [58], and some of the traditional methods [54,59], are included for comparison in Fig. 11. The unique combination of strength and ductility of the L-DED grade 91 steel sets it above other fabricated steels. It should be noted that some of the post-processing treatments of the T91 increase strength without losing much of the ductility (for example, [54;12]). A comparison to the L-DED product is not relevant, as the current research only focuses on the as-deposit state.

The superior properties obtained for the L-DED grade 91 steel are reasoned by the microstructure of the product, characterized with the heterogeneous dual-phase structure of a fine and coarse lath-type, saturated by dislocations, alongside the soft δ -phase. As mentioned earlier, the presence of δ -ferrite is known to result in a substantial loss of creep strength in the long-term creep condition [10]. Here, the volume fraction of the δ -ferrite, 15 %, is higher than that reported in the literature for the P91, fabricated using the traditional methods (example – [60]). On the other hand, chromium rich $M_{23}C_6$ carbides and other MX-type precipitates were not observed in the product (see Figure A 1- Appendix A of supplementary data). Although their presence contributes to strengthening, they also result in a remarkable loss of creep strength [9]. The combined effect of the non-negligible amount of the δ -ferrite coupled with the lack of deleterious particles on the applicability of grade 91 to nuclear applications is not known. Still, it should be recognized that the current status of L-DED grade 91 is to be con-

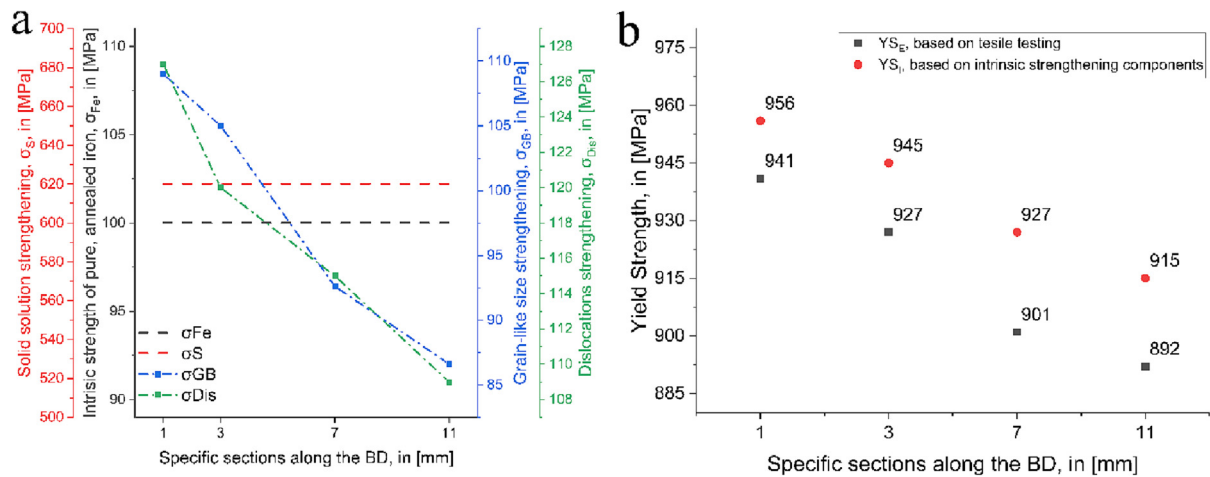


Fig. 10. (a) Intrinsic strengthening components and (b) the collective contributions of all strengthening components and the experimental tensile-yield Strength.

Table 4

Strengthening components and the integrated yield strength (YS_I) vs the experimental YS (YS_E) for the L-DED grade 91 steel.

Distance from the build platform [mm]	σ_{Fe} [MPa]	σ_S [MPa]	σ_{H-P} [MPa]	σ_P [MPa]	σ_{dis} [MPa]	YS _I [MPa]	YS _E [MPa]	$\Delta \sigma_{YS}$ [%]
1	100	620	109	NA	127	956	941	1.6
3	100	620	105	NA	120	945	927	1.9
7	100	620	92.6	NA	115	927.6	901	2.9
11	100	620	86.6	NA	109	915.6	892	2.6

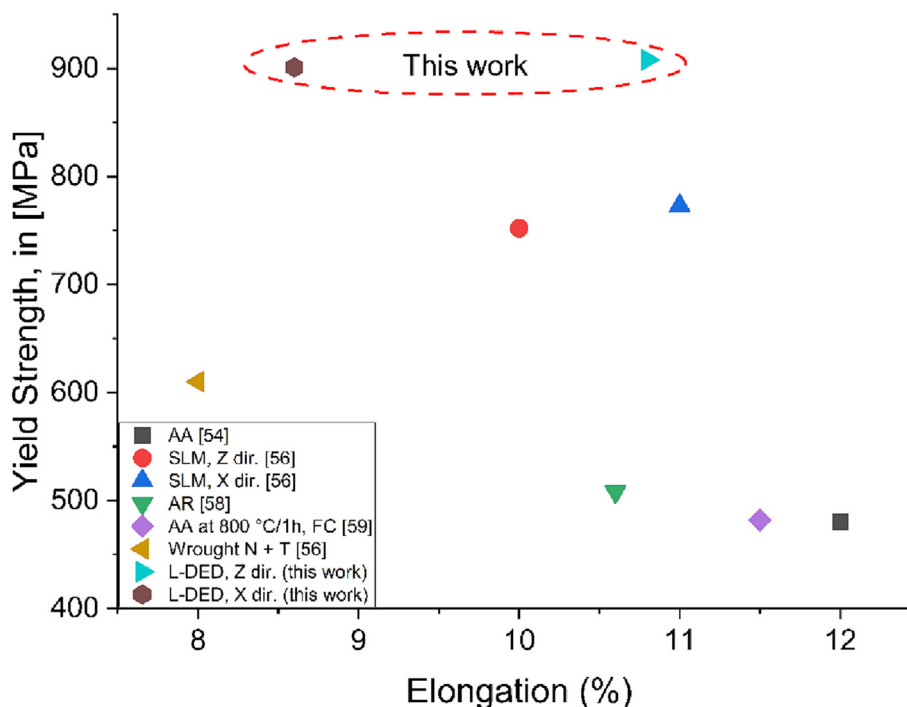


Fig. 11. Relationship between tensile yield strength and elongation of various grade 91 steels, conventionally processed and additively manufactured. Abbreviations - AA: as-annealing, AR: as-received, FC: furnace cool, SLM: selective laser melting.

sidered a good starting point for post-processing treatment. In [10] for example, the residual δ -ferrite dissolved completely after sequential normalizing heat treatment. It is, therefore, reasoned that with sequential optimized thermal post-processing treatment, the L-DED will meet the performance requirements.

In that context, it should also be acknowledged that a higher densification was found in the AM product farther away from the cold built platform. The majority of defects were metallurgical pores. These defects might act as a stress concentration region which might promote crack nucleation and propagation. Thus, it is necessary to develop fabrication or post-processing routines, such as thermo-mechanical treatments, that yield a uniformly densified structure, with reduced pore concentration while maintaining suitable mechanical properties.

5. Summary

This study provides an essential description of the process-structure-property relationships of the additively manufactured grade 91 steel with the objective of linking fabrication to performance. In this study, advanced electron diffraction characterization techniques coupled with macro and up to nano-scale mechanical properties testing were applied to assess the microstructure and to map the mechanical properties.

Major findings can be summarized as follows:

- The mechanical properties of the as-built L-DED-grade 91 product are superior to those of the traditional wrought material and as-deposited laser powder-bed fusion.
- A gradual decrease in the mechanical properties (tensile and nanoindentation hardness) was noted along the build direction. These changes were successfully explained in terms of several competing strengthening mechanisms. Two major strengthening components, the grain-like (σ_{GB}) and dislocation strengthening (σ_{Dis}) were responsible for the gradual softening with

increased distance from the cold build platform. Their activity was considered owing to the cold-build platform strategy and cyclic remelting effect stemming from the fast laser scans.

- Lastly, the presence of the δ -ferrite phase was addressed, suggesting sequential thermal post-processing treatment to be considered in order to dissolve this phase completely, thus placing the L-DED grade 91 as a promising candidate for nuclear applications.

Data availability

The raw/processed data required to reproduce these findings cannot be shared at this time as the data also forms part of an ongoing study

Declaration of Competing Interest

The authors declare that they have no known competing financial interests or personal relationships that could have appeared to influence the work reported in this paper.

Acknowledgments

This work was supported by the funding received from the DOE Office of Nuclear Energy's Nuclear Energy Enabling Technologies Program, as part of project 19-17206 of the Advanced Methods for Manufacturing Program.

S. Samuha acknowledges the partial support of the Pazy foundation.

Appendix A. Supplementary material

Supplementary data to this article can be found online at <https://doi.org/10.1016/j.matdes.2023.111804>.

References

- [1] R.L. Klueh, A.T. Nelson, Ferritic/martensitic steels for next-generation reactors, *J. Nucl. Mater.* 371 (2007) 37–52, <https://doi.org/10.1016/j.jnucmat.2007.05.005>.
- [2] A. Kohyama, A. Hishinuma, D.S. Gelles, R.L. Klueh, W. Dietz, K. Ehrlich, Low-activation ferritic and martensitic steels for fusion application, *J. Nucl. Mater.* 233–237 (1996) 138–147.
- [3] C. Fazio, A. Alamo, A. Almazouzi, S. De Grandis, D. Gomez-Briceno, J. Henry, L. Malerba, M. Rieth, European cross-cutting research on structural materials for Generation IV and transmutation systems, *J. Nucl. Mater.* 392 (2) (2009) 316–323.
- [4] D.S. Gelles, Microstructural development in reduced activation ferritic alloys irradiated to 200 dpa at 420°C, *J. Nucl. Mater.* 212–215 (1994) 714–719.
- [5] M.B. Toloczko, F.A. Garner, C.R. Eiholzer, Irradiation creep and swelling of the US fusion heats of HT9 and 9Cr-1Mo to 208 dpa at ~400°C, *J. Nucl. Mater.* 212–215 (1994) 604–607.
- [6] V.S. Agueev, V.N. Bykov, A.M. Dvoryashin, V.N. Golovanov, E.A. Medvendra, V. V. Romanev, V.K. Sharmardin, A.N. Vorobiev, N.H. Packan, R.E. Stoller, A.S. Kumar, Effects of Radiation on Mater. (1990), <https://doi.org/10.1520/stp1046-6>. 14th International Symposium (Volume 1).
- [7] Little E.A., Stoter L.P., Brager H.R., Perrin J.S., EFFECTS OF RADIATION ON MATERIALS, PROCEEDINGS OF THE 11TH INTERNATIONAL SYMPOSIUM., ASTM Special Technical Publication. (1982).
- [8] P.J. Maziasz, V.K. Sikka, Alloy Development for Irradiation Performance Semiannual Progress Report for Period Ending September 30, US Department of Energy Report DOE, ER-0045/15, Office of Fusion Energy, Washington, DC 102–116 (1985) 1985.
- [9] C. Panait, W. Bendick, A. Fuchsman, A.-F. Gourgues-Lorenzon, J. Besson, Study of the microstructure of the grade 91 steel after more than 100,000h of creep exposure at 600C, *Int. J. Press. Vessel. Pip.* 87 (2010) 326–335, <https://doi.org/10.1016/j.ijpvp.2010.03.017>.
- [10] S. Kobayashi, K. Sawada, T. Hara, H. Kushima, K. Kimura, The formation and dissolution of residual δ ferrite in ASME Grade 91 steel plates, *Mater. Sci. Eng. A* 592 (2014) 241–248, <https://doi.org/10.1016/j.msea.2013.10.058>.
- [11] R.L. Klueh, D.J. Alexander, Charpy impact toughness of martensitic steels irradiated in FFRF: effect of heat treatment, ASTM Special Technical Publication, Publ by ASTM, in, 1994, pp. 591–606.
- [12] Z.Q. Fan, T. Hao, S.X. Zhao, G.N. Luo, C.S. Liu, Q.F. Fang, The microstructure and mechanical properties of T91 steel processed by ECAP at room temperature, *J. Nucl. Mater.* 434 (2013) 417–421, <https://doi.org/10.1016/j.jnucmat.2012.12.009>.
- [13] A. Reichardt, R.P. Dillon, J.P. Borgonia, A.A. Shapiro, B.W. McEnerney, T. Momose, P. Hosemann, Development and characterization of Ti-6Al-4V to 304L stainless steel gradient components fabricated with laser deposition additive manufacturing, *Mater. Des.* 104 (2016) 404–413.
- [14] M.A. Bevan, A.A.H. Ameri, D. East, D.C. Austin, A.D. Brown, P.J. Hazell, J.P. Escobedo-Diaz, Mechanical Properties and Behavior of Additive Manufactured Stainless Steel 316L, in: Minerals, Metals and Materials Series, 2017. Doi: 10.1007/978-3-319-51382-9_63.
- [15] Z. Wang, T.A. Palmer, A.M. Beese, Effect of processing parameters on microstructure and tensile properties of austenitic stainless steel 304L made by directed energy deposition additive manufacturing, *Acta Mater.* 110 (2016). Doi: 10.1016/j.actamat.2016.03.019.
- [16] B. Baufeld, O.V.D. Biest, R. Gault, Additive manufacturing of Ti-6Al-4V components by shaped metal deposition: microstructure and mechanical properties, *Mater Des.* 31 (2010) S106–S111.
- [17] B. Tavlovich, A. Shirizly, R. Katz, EBW and LBW of additive manufactured H6Al4V products, *Weld J.* 97 (2018) 179s–190s, <https://doi.org/10.29391/2018.97.016>.
- [18] E.O. Olakanmi, R.F. Cochrane, K.W. Dalgarno, Densification mechanism and microstructural evolution in selective laser sintering of Al-12Si powders, *J. Mater. Process Technol.* 211 (1) (2011) 113–121.
- [19] T. DebRoy, H.L. Wei, J.S. Zuback, T. Mukherjee, J.W. Elmer, J.O. Milewski, A.M. Beese, A. Wilson-Heid, A. De, W. Zhang, Additive manufacturing of metallic components – Process, structure and properties, *Prog Mater Sci.* 92 (2018) 112–224.
- [20] C.H. Zhang, H. Zhang, C.L. Wu, S. Zhang, Z.L. Sun, S.Y. Dong, Multi-layer functional graded stainless steel fabricated by laser melting deposition, *Vacuum* 141 (2017) 181–187.
- [21] X.-H. Chen, B.o. Chen, X.u. Cheng, G.-C. Li, Z. Huang, Microstructure and properties of hybrid additive manufacturing 316L component by directed energy deposition and laser remelting, *J. Iron Steel Res. Int.* 27 (7) (2020) 842–848.
- [22] B.E. Carroll, R.A. Otis, J.P. Borgonia, J.-O. Suh, R.P. Dillon, A.A. Shapiro, D.C. Hofmann, Z.-K. Liu, A.M. Beese, Functionally graded material of 304L stainless steel and Inconel 625 fabricated by directed energy deposition: characterization and thermodynamic modeling, *Acta Mater.* 108 (2016) 46–54.
- [23] A.S. for T. and Materials, ASTM A387/A387M-17a: Standard Specification for Pressure Vessel Plates, Alloy Steel, Chromium-Molybdenum, ASTM International. i (2017). Doi: 10.1520/A0387_A0387M-17a
- [24] J.B. Pethica, W.C. Oliver, Mechanical properties of nanometre volumes of material: use of the elastic response of small area indentations, *MRS Proc.* 130 (1988) 13, <https://doi.org/10.1557/PROC-130-13>.
- [25] W.C. Oliver, G.M. Pharr, An improved technique for determining hardness and elastic modulus using load and displacement sensing indentation experiments, *J Mater Res.* 7 (6) (1992) 1564–1583.
- [26] D.L. Krumwiede, T. Yamamoto, T.A. Saleh, S.A. Maloy, G.R. Odette, P. Hosemann, Direct comparison of nanoindentation and tensile test results on reactor-irradiated materials, *J. Nucl. Mater.* 504 (2018) 135–143, <https://doi.org/10.1016/j.jnucmat.2018.03.021>.
- [27] H. Wang, A. Dhiman, H.E. Ostergaard, Y. Zhang, T. Siegmund, J.J. Kruzic, V. Tomar, Nanoindentation based properties of Inconel 718 at elevated temperatures: a comparison of conventional versus additively manufactured samples, *Int J Plast.* 120 (2019) 380–394, <https://doi.org/10.1016/j.ijplas.2019.04.018>.
- [28] J.T. Busby, M.C. Hash, G.S. Was, The relationship between hardness and yield stress in irradiated austenitic and ferritic steels, *J. Nucl. Mater.* 336 (2–3) (2005) 267–278.
- [29] K. Mao, H. Wang, Y. Wu, V. Tomar, J.P. Wharry, Microstructure-property relationship for AISI 304/308L stainless steel laser weldment, *Mater. Sci. Eng. A* 721 (2018) 234–243.
- [30] F. Bachmann, R. Hielscher, H. Schaeben, Texture analysis with MTEX- Free and open source software toolbox, *Solid State Phenom.* 160 (2010) 63–68.
- [31] J.-Y. Kang, S.-J. Park, M.-B. Moon, Phase analysis on dual-phase steel using band slope of electron backscatter diffraction pattern, *Microsc. Microanal.* 19 (S5) (2013) 13–16.
- [32] F. Niessen, T. Nyssönen, A.A. Gazder, R. Hielscher, Parent grain reconstruction from partially or fully transformed microstructures in MTEX, n.d.
- [33] O. Muránsky, L. Balogh, M. Tran, C.J. Hamelin, J.S. Park, M.R. Daymond, On the measurement of dislocations and dislocation substructures using EBSD and HRSD techniques, *Acta Mater.* 175 (2019) 297–313, <https://doi.org/10.1016/j.actamat.2019.05.036>.
- [34] J.F. Nye, Some geometrical relations in dislocated crystals, *Acta Metall.* 1 (2) (1953) 153–162.
- [35] W. Pantleon, Resolving the geometrically necessary dislocation content by conventional electron backscattering diffraction, *Scr Mater.* 58 (2008) 994–997, <https://doi.org/10.1016/j.scriptamat.2008.01.050>.
- [36] G.M. Guttman, S. Samuha, R. Gertner, B. Ostrach, S. Haroush, Y. Gelbstein, The Thermo-Mechanical Response of GeTe under Compression, *Materials.* 15 (17) (2022) 5970.
- [37] L. Cui, S. Jiang, J. Xu, R.L. Peng, R.T. Mousavian, J. Moverare, Revealing relationships between microstructure and hardening nature of additively manufactured 316L stainless steel, *Mater Des.* 198 (2021), <https://doi.org/10.1016/j.matdes.2020.109385> 109385.
- [38] O. Muránsky, L. Balogh, M. Tran, C.J. Hamelin, J.-S. Park, M.R. Daymond, On the Measurement of Dislocations and Dislocation Structures using EBSD and HRSD Techniques, n.d.
- [39] A. Strang, J.D. Cawley, G.W. Greenwood, Microstructural stability of creep resistant alloys for high temperature plant applications, in: 1997.
- [40] C. Heintze, F. Bergner, S. Akhmadaliev, E. Altstadt, H.-Z. Dresden -Rossendorf, Ion irradiation combined with nanoindentation as a screening test procedure for irradiation hardening, n.d.
- [41] G.M. Pharr, E.G. Herbert, Y. Gao, The Indentation Size Effect: A Critical Examination of Experimental Observations and Mechanistic Interpretations, *Annu Rev Mater Res.* 40 (2010) 271–292. Doi: 10.1146/annurev-matsci-070909-104456.
- [42] W.D. Nix, H. Gao, Indentation size effects in crystalline materials: A law for strain gradient plasticity, *J Mech Phys Solids.* 46 (1998) 411–425. Doi: Doi: 10.1016/S0022-5096(97)00086-0.
- [43] H. Zhang, B. Long, Y. Dai, Metallography studies and hardness measurements on ferritic/martensitic steels irradiated in STIP, *J. Nucl. Mater.* 377 (2008) 122–131, <https://doi.org/10.1016/j.jnucmat.2008.02.037>.
- [44] J. Liu, J. Wilson, M. Strangwood, C.L. Davis, A. Peyton, J. Parker, Electromagnetic evaluation of the microstructure of Grade 91 tubes/pipes, *Int. J. Press. Vessel. Pip.* 132–133 (2015) 65–71, <https://doi.org/10.1016/j.ijpvp.2015.05.009>.
- [45] Z. Tong, Y. Dai, The microstructure and tensile properties of ferritic/martensitic steels T91, Eurofer-97 and F82H irradiated up to 20dpa in STIP-III, *J. Nucl. Mater.* 398 (2010) 43–48, <https://doi.org/10.1016/j.jnucmat.2009.10.008>.
- [46] S. Morito, H. Yoshida, T. Maki, X. Huang, Effect of block size on the strength of lath martensite in low carbon steels, *Mater. Sci. Eng. A* 438–440 (2006) 237–240, <https://doi.org/10.1016/j.msea.2005.12.048>.
- [47] A.J. Wilkinson, D. Randman, Determination of elastic strain fields and geometrically necessary dislocation distributions near nanoindentations using electron back scatter diffraction, *Phil. Mag.* 90 (2010) 1159–1177, <https://doi.org/10.1080/14786430903304145>.
- [48] P. Lehto, Adaptive domain misorientation approach for the EBSD measurement of deformation induced dislocation sub-structures, *Ultramicroscopy* 222 (2021), <https://doi.org/10.1016/j.ultramic.2021.113203> 113203.
- [49] J. Jiang, T.B. Britton, A.J. Wilkinson, Measurement of geometrically necessary dislocation density with high resolution electron backscatter diffraction: effects of detector binning and step size, *Ultramicroscopy* 125 (2013) 1–9, <https://doi.org/10.1016/j.ultramic.2012.11.003>.
- [50] J. Oñoro, Martensite microstructure of 9–12%Cr steels weld metals, *J. Mater. Process Technol.* 180 (1–3) (2006) 137–142.
- [51] E.N. Tembwa, Softening response of as-normalized and cryogenic-soaked P91 martensitic steels, 2018.
- [52] G. Krauss, Martensite in steel: strength and structure, *Mater. Sci. Eng. A* 273–275 (1999) 40–57.

- [53] Z. Shang, J. Ding, C. Fan, M. Song, J. Li, Q. Li, S. Xue, K.T. Hartwig, X. Zhang, Tailoring the strength and ductility of T91 steel by partial tempering treatment, *Acta Mater.* 169 (2019) 209–224, <https://doi.org/10.1016/j.actamat.2019.02.043>.
- [54] M. Song, C. Sun, Z. Fan, Y. Chen, R. Zhu, K.Y. Yu, K.T. Hartwig, H. Wang, X. Zhang, A roadmap for tailoring the strength and ductility of ferritic/martensitic T91 steel via thermo-mechanical treatment, *Acta Mater.* 112 (2016) 361–377, <https://doi.org/10.1016/j.actamat.2016.04.031>.
- [55] Z. Jiang, Z. Guan, J. Lian, Effects of microstructural variables on the deformation behaviour of dual-phase steel, *Mater. Sci. Eng. A* 190 (1995) 55–64, [https://doi.org/10.1016/0921-5093\(94\)09594-M](https://doi.org/10.1016/0921-5093(94)09594-M).
- [56] H.K.D.H. Bhadeshia, S.R. Honeycombe, 4 - The Effects of Alloying Elements on Iron-Carbon Alloys, in: H.K.D.H. Bhadeshia, S.R. Honeycombe (Eds.), *Steels*, (Third Edition), Butterworth-Heinemann, Oxford, 2006, pp. 71–93, <https://doi.org/10.1016/B978-075068084-4/50006-6>.
- [57] B.B. He, B. Hu, H.W. Yen, G.J. Cheng, Z.K. Wang, H.W. Luo, M.X. Huang, High dislocation density-induced large ductility in deformed and partitioned steels, *Science* 357 (1979) 1029–1032, <https://doi.org/10.1126/science.aan0177>.
- [58] B.P. Eftink, D.A. Vega, O. El Atwani, D.J. Sprouster, Y.S.J. Yoo, T.E. Steckley, E. Aydogan, C.M. Cady, M. Al-Sheikhly, T.J. Lienert, S.A. Maloy, Tensile properties and microstructure of additively manufactured Grade 91 steel for nuclear applications, *J. Nucl. Mater.* 544 (2021) 152723.
- [59] M. Song, C. Sun, Y. Chen, Z. Shang, J. Li, Z. Fan, K.T. Hartwig, X. Zhang, Grain refinement mechanisms and strength-hardness correlation of ultra-fine grained grade 91 steel processed by equal channel angular extrusion, *Int. J. Press. Vessel. Pip.* 172 (2019) 212–219, <https://doi.org/10.1016/j.ijpvp.2019.03.025>.
- [60] A.B. Zala, N.I. Jamnapara, V.J. Badheka, C. Sasmal, S. Sam, M. Ranjan, Delta (δ) Ferrite Formation in the Welds of Aluminized 9Cr-1Mo Steels, *Metallography, Microstructure, and Anal.* 8 (2019) 256–262, <https://doi.org/10.1007/s13632-019-00528-1>.